

IDEALIZED GLOBAL MODELS OF ACCRETION DISKS WITH STRONG TOROIDAL MAGNETIC FIELDS

MINGHAO GUO (郭明浩)  *, ELIOT QUATAERT  , JONATHAN SQUIRE  , PHILIP F. HOPKINS  , AND JAMES M. STONE   ¹Department of Astrophysical Sciences, Princeton University, Princeton, NJ 08544, USA²Physics Department, University of Otago, 730 Cumberland St., Dunedin 9016, New Zealand³TAPIR, Mailcode 350-17, California Institute of Technology, Pasadena, CA 91125, USA and⁴School of Natural Sciences, Institute for Advanced Study, 1 Einstein Drive, Princeton, NJ 08540, USA

Version June 12, 2025

ABSTRACT

We present global magnetohydrodynamic (MHD) simulations of accretion disks with a strong toroidal magnetic field using an equation of state that fixes the gas thermal scale height. The disk forms from the inflow of a rotating magnetized gas cloud with a toroidal magnetic field. We find that the system maintains a moderately strong mean azimuthal field in the midplane, with plasma- $\beta \sim 1$, trans-Alfvénic fluctuations, and large accretion stresses $\alpha \sim 0.1$. The azimuthal field in the disk is continuously escaping along the vertical direction but is also replenished via a local dynamo. The inflowing gas initially forms a strongly magnetized Keplerian disk with $\beta \ll 1$ and $\alpha \gg 1$. The disk gradually collapses from the inside out over $\sim 50 - 80$ orbits to form a moderately magnetized disk with $\beta \sim 1$ and $\alpha \sim 0.1$. Radial advection of azimuthal magnetic field can maintain $\beta \lesssim 1$ exterior to the circularization radius but not inside of it. Inclusion of a net initial vertical magnetic field can lead to an even more strongly magnetized disk midplane, consistent with previous work. When the gas thermal scale is not resolved ($\lesssim 4$ cells per thermal scale height), however, the disk remains highly magnetized with $\beta \ll 1$. We discuss our results in the context of related shearing box simulations and other global disk simulations. The level of angular momentum transport found here is consistent with that inferred observationally in dwarf novae and X-ray transient outbursts, unlike simulations of weakly magnetized accretion disks.

Subject headings: Accretion (14) — Black holes (162) — Supermassive black holes (1663) — Active galactic nuclei (16) — Quasars(1319) — X-ray binary stars(1811) — Astrophysical fluid dynamics (101) — Magnetohydrodynamics (1964) — Magnetohydrodynamical simulations (1966)

1. INTRODUCTION

The classic analytic model of accretion disks is the “ α -disk” model proposed in the seminal work by [Shakura & Sunyaev \(1973\)](#), where a parameter α quantifies the effective viscosity and thus the rate of angular momentum transport. For hotter systems in which the accreting plasma is ionized, angular momentum transport is believed to be dominated by magnetic stresses produced by either winds ([Blandford & Payne 1982](#)) or local turbulence induced by the magnetorotational instability (MRI; [Balbus & Hawley 1991](#)). In local and global numerical simulations, the angular momentum transport produced by the MRI corresponds to α between $\simeq 0.001$ and $\simeq 1$, depending on the physical parameters and resolution, with net vertical magnetic flux leading to the larger values of α ([Hawley et al. 1995](#); [Stone et al. 1996](#); [Bai & Stone 2013](#); [Ryan et al. 2017](#)). Transport inferred observationally in the outbursts of dwarf novae and X-ray binaries favors $\alpha \sim 0.1 - 0.3$ ([King et al. 2007](#); [Tetarenko et al. 2018](#)), corresponding to a strongly magnetized accretion disk. In addition, magnetic pressure support can stabilize the disk against thermal and viscous instabilities ([Frank et al. 2002](#); [Begelman & Pringle 2007](#)), which would otherwise be generic in the inner parts of luminous black hole and neutron star accretion disks (but there is little direct phenomenological evidence for such instabilities). Strong magnetic pressure

support also produces lower gas densities for a given accretion rate, making the disks in AGN less susceptible to gravitational instability and star formation ([Shlosman & Begelman 1987](#); [Goodman 2003](#); [Johansen & Levin 2008](#)).

The most widely studied models of strongly magnetized accretion disks are those with net vertical magnetic fields. In local shearing box simulations with an initial net vertical flux (NVF) with plasma- $\beta \lesssim 10^3$ (the ratio of thermal to magnetic pressure), the MRI saturates with stronger magnetic fields and more efficient angular momentum transport; for initial $\beta \lesssim 100$ the midplane of the disk becomes magnetically dominated ([Bai & Stone 2013](#); [Salvesen et al. 2016](#)). Similar results are also found in global simulations ([Mishra et al. 2020](#); [Kudoh et al. 2020](#)) where significant angular momentum transport by MHD winds can play an important role as well ([Zhu & Stone 2018](#)) (see [Lesur et al. 2013](#) for the role of winds in the shearing box).

An alternative to disks with strong vertical magnetic fields is those with strong toroidal magnetic fields. Indeed, a series of global numerical simulations have found accretion disks dominated by strong, superthermal toroidal magnetic fields with $\beta \ll 1$ and $\alpha \gtrsim 1$ due to the accompanying magnetic stress ([Machida et al. 2006](#); [Gaburov et al. 2012](#); [Sadowski 2016](#); [Hopkins et al. 2024a,b](#); [Guo et al. 2024](#); [Hopkins et al. 2025](#); [Wang et al. 2025](#); [Jiang et al. 2025](#)). Theoretically, such disks may form robustly if the disk forms via compression along

* mhguo@princeton.edu

the rotation axis of the system (this conserves B_z but amplifies B_ϕ). However, whether or not such a configuration can in fact be maintained in the face of buoyant loss of magnetic field (Parker 1958) has been the subject of debate. Johansen & Levin (2008) found that zero-net-vertical-flux (ZNVF) shearing boxes could maintain a $\beta \sim 1$ toroidal field mediated by a Parker instability-driven dynamo; however, their vertical boundary conditions precluded azimuthal magnetic flux loss and Salvesen et al. (2016) and Fragile & Sadowski (2017) showed numerical examples where strong toroidal magnetic fields cannot be sustained in the presence of Parker-instability mediated loss of magnetic flux.

Squire et al. (2024) recently reinvestigated the strongly magnetized disk in ZNVF shearing box simulations with toroidal magnetic fields. They found two regimes of accretion: (1) a weakly magnetized state (the "high β state") with $\beta \sim 100$ and $\alpha \sim 0.01$ (as in previous work) and (2) a regime of strongly magnetized accretion (the "low β state") characterized by a $\beta \sim 1$ midplane dominated by a coherent azimuthal field with strong turbulence and large accretion stress $\alpha \sim 1$. In the latter regime, the loss of magnetic flux due to magnetic buoyancy is compensated for by a local dynamo, maintaining the $\beta \sim 1$ state. This shearing box result bears some resemblance to the global results (Gaburov et al. 2012; Hopkins et al. 2024a; Guo et al. 2024) except that in the latter cases the magnetic field is much stronger with a plasma- $\beta \ll 1$. The origin of this important quantitative difference is unclear.

To understand what conditions are required to support a superthermal magnetic field, we undertake idealized global simulations of accretion disks with strong toroidal magnetic fields. We intentionally choose a simple model problem in which the thermodynamics of the gas is specified by a locally (at a given radius) isothermal equation of state corresponding to a fixed disk aspect ratio, i.e., a fixed scale height relative to the local disk radius. As we shall show, we find a regime with $\beta \sim 1$ and $\alpha \sim 0.1$, similar in many respects to the low β state in Squire et al. (2024). Because of the uncertainty in the literature about the existence and properties of $\beta \lesssim 1$ toroidally dominated disk without net vertical flux, we intentionally provide a detailed, and we hope, comprehensive analysis of the disk properties we find here and their dependence on resolution.

The rest of this article is organized as follows. In Section 2 we describe the numerical method we adopt. Section 3 presents the results of the MHD simulations. In Section 4, we conclude and discuss the implications of our results.

2. METHOD

We perform magnetohydrodynamic simulations using AthenaK (Stone et al. 2024), a performance portable version of the Athena++ (Stone et al. 2020) code implemented using the Kokkos library (Trott et al. 2021). AthenaK provides a variety of reconstruction methods, Riemann solvers, and integrators for solving the MHD equations. The adaptive mesh refinement (AMR) in AthenaK allows us to flexibly achieve a high resolution and good performance over an extremely large dynamic range. In our simulations, we adopt the piecewise linear (PLM) reconstruction method, the HLLD Riemann solver, and the RK2 time integrator to solve the MHD equations.

TABLE 1
LIST OF RUNS AND THEIR PARAMETERS.

Model Name	h	β_ϕ	β_z	Cells/Level	$hr/\Delta x$	$t_{\text{run}} [10^3 t_0]$
h05n256 (fid.)	0.05	1	∞	256^3	6.4	0-60
h05n512t3 ^a	0.05	1	∞	512^3	12.8	30-33
h05n128	0.05	1	∞	128^3	3.2	0-60
h05n64	0.05	1	∞	64^3	1.6	0-60
h10n256	0.1	1	∞	256^3	12.8	0-15
h10n128	0.1	1	∞	128^3	6.4	0-30
h10n64	0.1	1	∞	64^3	3.2	0-30
h02n256	0.025	1	∞	256^3	3.2	0-15
h02n128	0.025	1	∞	128^3	1.6	0-30
h02n64	0.025	1	∞	64^3	0.8	0-30
h01n256	0.0125	1	∞	256^3	1.6	0-15
h01n128	0.0125	1	∞	128^3	0.8	0-30
h01n64	0.0125	1	∞	64^3	0.4	0-30
h05b10	0.05	0.1	∞	256^3	6.4	0-30
h05b1z1	0.05	1	2	256^3	6.4	0-30
h05b0z1	0.05	∞	2	256^3	6.4	0-30
h05ppm	0.05	1	∞	256^3	6.4	0-10
h05n64-256	0.05	1	∞	64^3	1.6	15-20
h05n64-256-64	0.05	1	∞	64^3	1.6	20-30
h05n512t0 ^b	0.05	1	∞	512^3	12.8	4-7

NOTE. — Main parameters of simulations in this work, listed approximately in the order in which they are discussed. Here $\beta_\phi \equiv \int P_{\text{gas}} dV / \int B_\phi^2 / 2 dV$ and $\beta_z \equiv \int P_{\text{gas}} dV / \int B_z^2 / 2 dV$. The model h05n256 is the fiducial run. The value of $hr/\Delta x$ indicates a typical resolution in terms of thermal scale height. The actual resolution varies by a factor of 2 across the boundary of mesh refinement and is shown in Fig. 14 in Appendix A. The model h05ppm uses the piecewise parabolic (PPM) reconstruction method.

^a Restarts from model h05n256 at $t/t_0 = 30,000$ and runs to $t/t_0 = 33,000$.

^b Restarts from model h05n256 at $t/t_0 = 4000$ and runs to $t/t_0 = 7000$.

The ideal MHD equations we solve are

$$\frac{\partial \rho}{\partial t} + \nabla \cdot (\rho \mathbf{v}) = 0, \quad (1)$$

$$\frac{\partial \rho \mathbf{v}}{\partial t} + \nabla \cdot (P_{\text{tot}} \mathbf{I} + \rho \mathbf{v} \mathbf{v} - \mathbf{B} \mathbf{B}) = \rho \mathbf{g}, \quad (2)$$

$$\frac{\partial E}{\partial t} + \nabla \cdot [(E + P_{\text{tot}}) \mathbf{v} - \mathbf{B} (\mathbf{B} \cdot \mathbf{v})] = \rho \mathbf{g} \cdot \mathbf{v}, \quad (3)$$

$$\frac{\partial \mathbf{B}}{\partial t} - \nabla \times (\mathbf{v} \times \mathbf{B}) = 0, \quad (4)$$

where ρ is the gas density, \mathbf{v} is the velocity, $P_{\text{tot}} = P_{\text{gas}} + P_{\text{mag}}$ with $P_{\text{gas}} = \rho T$ the gas pressure and $P_{\text{mag}} = B^2/2 = \mathbf{B} \cdot \mathbf{B}/2$ the magnetic pressure, $\mathbf{g} = -GM\mathbf{r}/r^3$ is the gravitational acceleration, $E = E_{\text{int}} + \rho v^2/2 + B^2/2$ is the total energy density with $E_{\text{int}} = P_{\text{gas}}/(\gamma - 1)$ the internal energy density where $\gamma = 1.4$. The adiabatic index γ is only used in the Riemann solver. The equation of state we use is locally isothermal by fixing the temperature at all times to be the initial value $T = T_{\text{init}}$ (described below). These equations are written in units such that the magnetic permeability $\mu_m = 1$. The Alfvén speed is $v_A \equiv B/\sqrt{\rho}$ in such units.

The initial conditions for our simulations are a cloud of gas with constant density and angular momentum and a locally isothermal equation of state in which the temperature depends on cylindrical radius. Over time this gas cloud flows inwards, circularizes, and forms a disk with an initially strong toroidal magnetic field. More specifically, the initial gas density, tem-

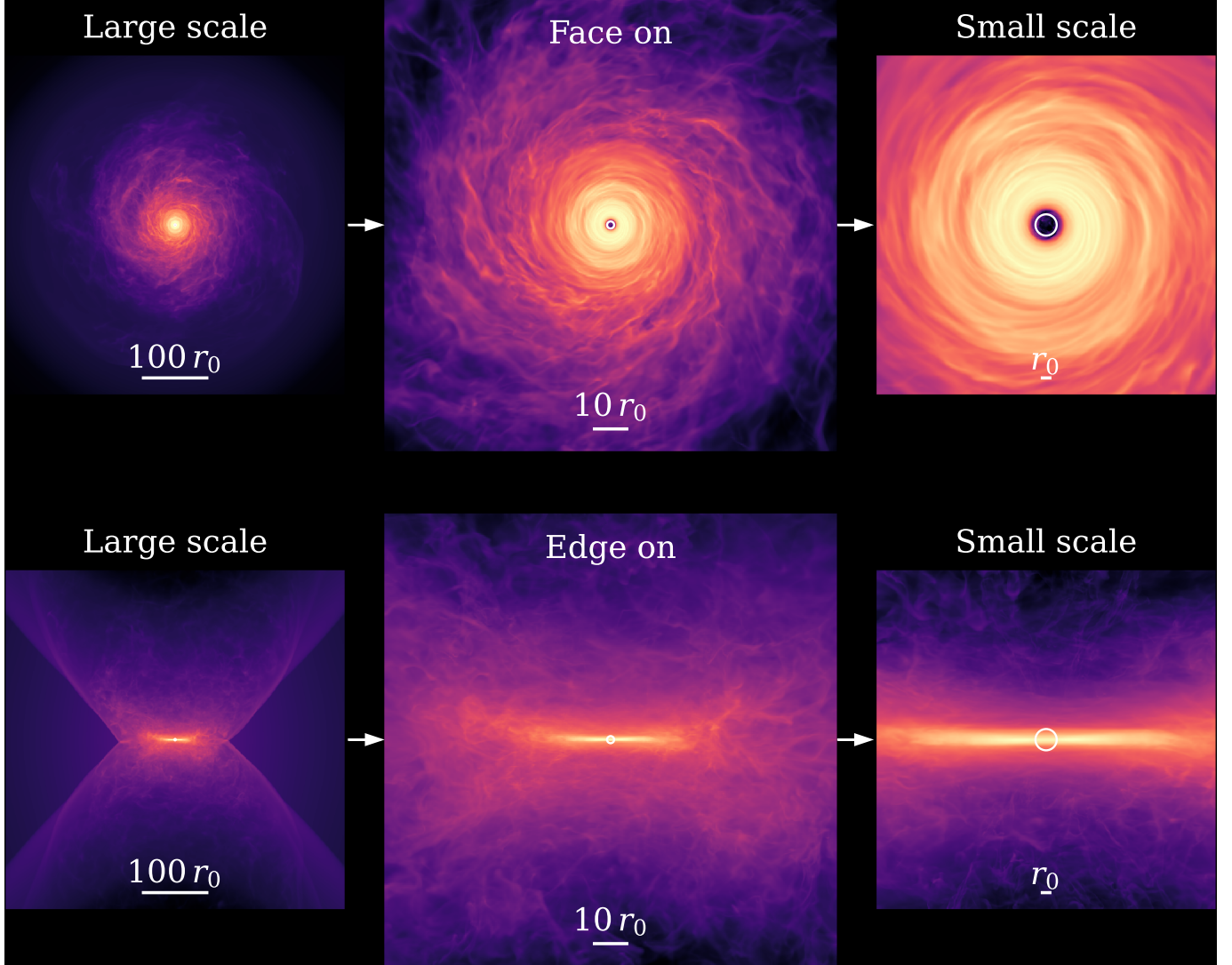


FIG. 1.— Face-on (top) and edge-on (bottom) view of surface density on a logarithmic scale ($h = 0.05$, model h05n512t3 at $t/t_0 = 3.3 \times 10^4$). The material from large scales ($\gtrsim 100 r_0$) inflows radially and circularizes at $R_{\text{circ}} = 16 r_0$, forming a rotationally supported turbulent accretion disk.

perature, and velocity are set using cylindrical coordinates by

$$\rho_{\text{init}}(R, z) = \begin{cases} \rho_0 & \text{if } R \geq R_{\text{circ}}, \\ \rho_{\text{floor}} \rho_0^f & \text{if } R_{\text{inner}} \leq R < R_{\text{circ}}, \\ \rho_{\text{floor}} & \text{otherwise,} \end{cases} \quad (5)$$

$$T_{\text{init}}(R, z) = \max \left(h^2 \frac{GM}{R}, T_{\text{inf}} \right), \quad (6)$$

$$v_{\phi, \text{init}}(R, z) = \begin{cases} \frac{j_{\text{circ}}}{R} & \text{if } R \geq R_{\text{circ}}, \\ \frac{j_{\text{circ}}}{R} \left(\frac{R}{R_{\text{circ}}} \right)^{1/2} & \text{otherwise,} \end{cases} \quad (7)$$

where

$$f = \frac{\ln(R/R_{\text{inner}})}{\ln(R_{\text{circ}}/R_{\text{inner}})}, \quad (8)$$

so that the density smoothly changes from ρ_{floor} to ρ_0 . Here h is a free parameter controlling the thermal scale height $H_{\text{th}} = \sqrt{2}hR$ and $j_{\text{circ}} = j_{\text{K}}(R_{\text{circ}}) = \sqrt{GMR_{\text{circ}}}$ is the Keplerian angular momentum at the specified circularization radius R_{circ} . The temperature is set in order to enforce a thermal

scale height in the roughly Keplerian portion of the flow that is proportional to the cylindrical radius.

The magnetic field is initialized by $\mathbf{B} = \nabla \times \mathbf{A}$, where the vector potential is $\mathbf{A} = A_{z, \text{init}} \hat{z}$ with

$$A_{z, \text{init}} = \begin{cases} -A_0(R - R_{\text{circ}}) & \text{if } R \geq R_{\text{circ}}, \\ 0 & \text{otherwise,} \end{cases} \quad (9)$$

to construct a purely toroidal field outside R_{circ} . The vector potential normalization A_0 is chosen to set a specified mean plasma- $\beta_{\phi} = \int P_{\text{gas}} dV / \int B_{\phi}^2 / 2dV$ at large radii in the initial condition. We also run simulations with net vertical flux in addition to the toroidal field. In those runs, we add a uniform vertical magnetic field B_z across the full domain with a specified mean $\beta_z \equiv \int P_{\text{gas}} dV / \int B_z^2 / 2dV$.

In all runs, we use $G = M = 1$ and an inner radius of the domain of $r_0 = 1$. The corresponding time unit is $t_0 = (r_0^3/GM)^{1/2} = 1$. We fix the parameters of the initial conditions to be $\rho_0 = 1$, $\rho_{\text{floor}} = 10^{-4}$, $R_{\text{circ}} = 16 r_0$, $R_{\text{inner}} = 8 r_0$, $T_{\text{inf}} = 10^{-5}$. For the fiducial run we set $h = 0.05$ and

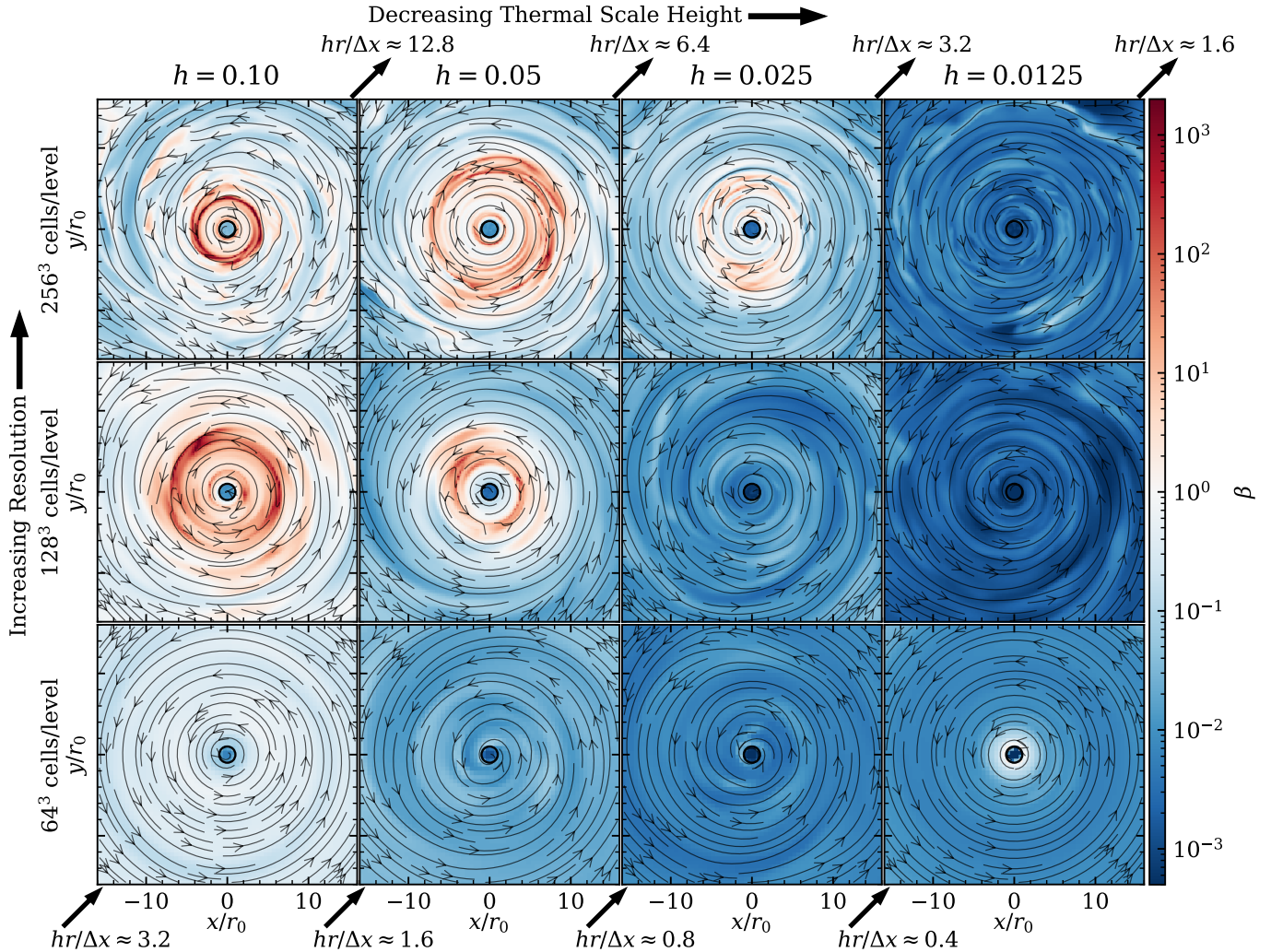


FIG. 2.— Slices of midplane β and magnetic field lines when the system is in a quasi-steady state for different thermal scale height and resolution. The time is $15k t_0$ for the run with 256^3 cells/level and $30k t_0$ for others. The diagonal panels from lower left to upper right show the same relative resolution in terms of cells per thermal scale height. The midplane $\beta \sim 1$ if the thermal scale height is resolved with $hr/\Delta x \gtrsim 4$ and $\beta \ll 1$ if the thermal scale height is not resolved.

the vector potential normalization A_0 such that the plasma is initially magnetized with $\beta_\phi = 1$ at large radii (note that this corresponds to an initial magnetic energy that is small compared to the kinetic energy of the free-falling gas that develops as the simulations progresses, because $T_{\text{init}}/(GM/R) \propto h^2$). For the cases with vertical flux, we set $\beta_z = 2$ such that the initial average magnetic energy along all three directions x , y , and z is the same. This means that the initial toroidal field is $B_\phi = \sqrt{2}B_z$ for $R > R_{\text{circ}}$. For $R < R_{\text{circ}}$, the vertical β is initially very small because the gas density is very low, but can increase significantly later due to the inflow from large radii. These initial conditions are asymptotically a uniform medium on large scales. We do not add any perturbations to the initial conditions. The turbulence that emerges in the simulations is generated from machine-level noise.

We fix the outer boundary conditions to be the initial conditions. The fixed outer boundary conditions have negligible effects on the accretion flow at smaller radii because of the large separation of spatial and time scales. For the inner boundary ($r < r_0 = 1$), we adopt a vacuum sink by resetting a fixed density $\rho_{\text{sink}} = \rho_{\text{floor}} = 10^{-4}$, temperature $T_{\text{sink}} = 10^{-4}$, and zero velocity every time step. To avoid a large Alfvén speed

within the sink, we apply a ceiling $v_{A,\text{ceil}} = 2v_K(r_{\text{in}}) = 2$ where $v_K(r) \equiv \sqrt{GM/r}$ is the local Keplerian velocity. We apply the ceiling by increasing the density after applying the density sink without changing the magnetic field.

The simulations adopt a cubic box of size $[-2^{12}, 2^{12}]^3 = [-4096, 4096]^3 r_0^3$. The root grid is a cube of 256^3 cells in the fiducial run, which is divided into $4 \times 4 \times 4$ mesh blocks, with each mesh block being a cube of 64^3 cells. At each level of mesh refinement, we double the resolution by refining the central $2 \times 2 \times 2$ parent mesh blocks into $4 \times 4 \times 4$ child mesh blocks. We apply 9 levels of mesh refinement with the finest resolution of $\Delta x_{\text{min}} = r_0/16$ covering a domain of $[-8, 8]^3 r_0^3$. Each level is resolved with 256^3 cells. The details of the resolution are presented in Appendix A.

After evolving the fiducial case for $3 \times 10^4 t_0$, we restart the simulations and double the resolution everywhere. This run thus has a resolution of 512^3 cells per level with $\Delta x_{\text{min}} = r_0/32$, and we run it for an extra $3 \times 10^3 t_0$ for the convergence study. In addition, we explore a parameter space of $h \in [0.1, 0.05, 0.025, 0.0125]$ and resolution of $[256^3, 128^3, 64^3]$ cells per mesh refinement level to understand how the results

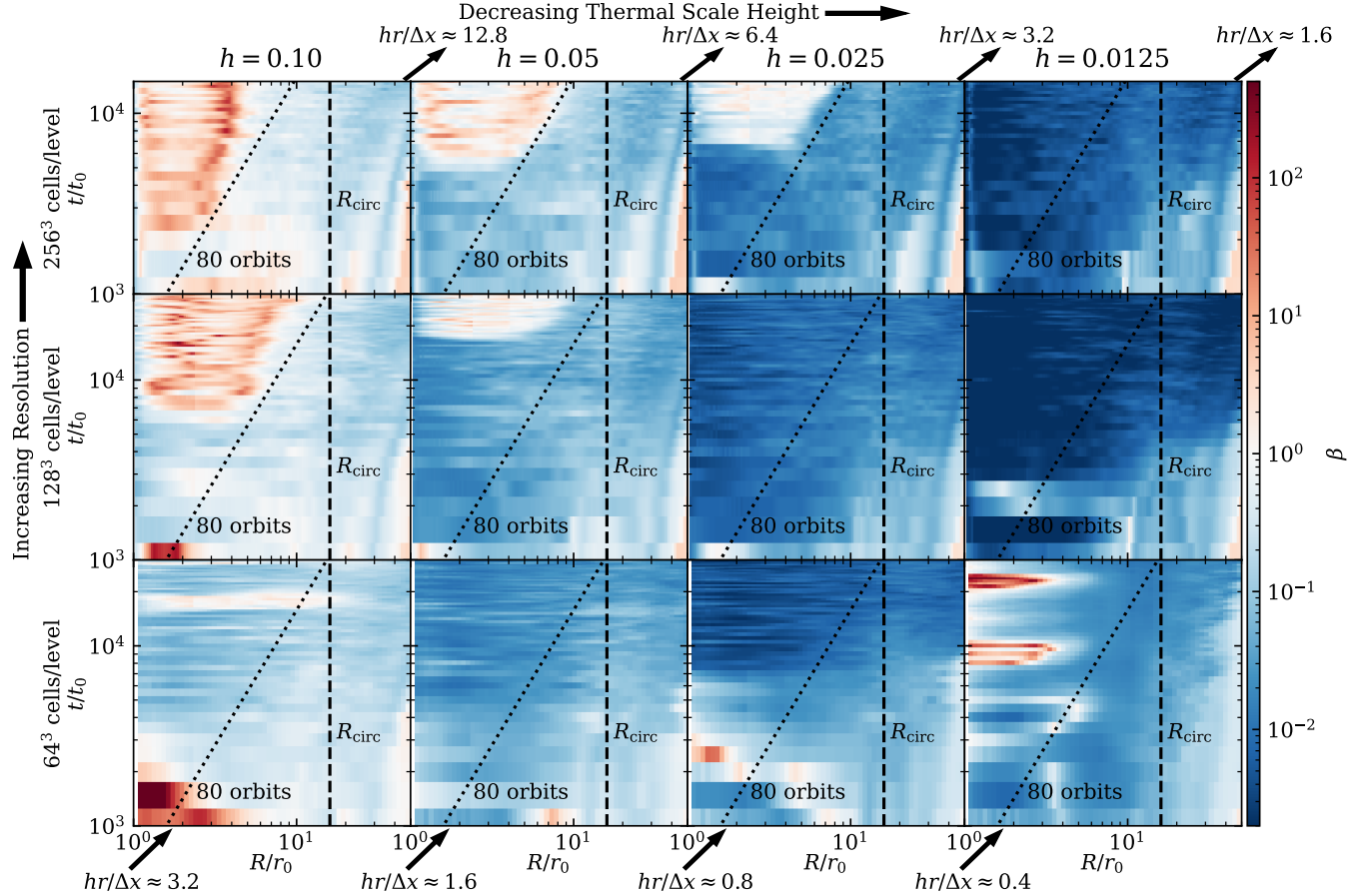


FIG. 3.— Space-time diagram of azimuthally averaged midplane β for the runs shown in Fig. 2. The black dashed lines mark the circularization radius $R_{\text{circ}} = 16 r_0$. The black dotted lines mark the time when the evolution time is 80 orbital periods at the corresponding radius. The diagonal panels from lower left to upper right show the same relative resolution in terms of cells per thermal scale height. The H_{th} -unresolved cases maintain $\beta \ll 1$ while the H_{th} -resolved cases gradually transition to a disk with midplane $\beta \sim 1$ after $\sim 50 - 80$ orbits at the corresponding radius.

change with the resolution relative to the thermal scale height. The finest resolution in each case is $\Delta x_{\min} = 1/16, 1/8, 1/4 r_0$, respectively. Furthermore, we run a series of tests varying the initial magnetic field strength, structure, numerical method, and mesh refinement and derefinement, which are presented in Section 3.6. The main parameters of all the runs are summarized in Table 1. The set of runs costs about 200,000 GPU hours in total.

3. RESULTS

Fig. 1 illustrates the gas morphology of the highest resolution model h05n512t3 from large to small scales at the end of the simulation ($t/t_0 = 3.3 \times 10^4$). The material from large scales ($\gtrsim 100 r_0$) inflows radially and circularizes around R_{circ} due to the initial angular momentum, forming a rotationally supported turbulent accretion disk. Below we present the results of the simulations with a focus on the disk within $\sim R_{\text{circ}}$.

3.1. Magnetic transition of the accretion disk

Fig. 2 summarizes the magnetic state of the disks with $z = 0$ slices of plasma- β when the system is in a quasi-steady state for a set of runs varying the thermal scale height and resolution. The diagonal panels from lower left to upper right show the same relative resolution in terms of number of cells per thermal scale height. There are two classes of solutions for midplane β depending on the resolution relative to the thermal scale

height. If the thermal scale height is not resolved, the disk is strongly magnetized with $\beta \ll 1$. Instead, if the disk is resolved with $hr/\Delta x \gtrsim 3$ on average (i.e., $\gtrsim 4$ cells per H_{th}), the disk begins to be moderately magnetized with $\beta \sim 1$. The disks with the same relative resolution show similar behaviors. We note that the $\beta \sim 1$ midplane is also very different from the traditional disk with ZNVF. Instead, it is similar to the low β state in Squire et al. (2024).

Space-time diagrams of the azimuthally averaged midplane plasma- β for the same runs are shown in Fig. 3. The H_{th} -unresolved cases show a persistent $\beta \ll 1$. The only exception is the case h01n64, where the disk transitions to a $\beta \sim 1$ occasionally, likely because the resolution is too low ($hr/\Delta x \approx 0.4$) to resolve the accretion disk. If the thermal scale height is resolved, during the early stage of the evolution, the disk still shows a midplane $\beta \ll 1$ which is similar to the unresolved case. However, it gradually transitions to a disk with midplane $\beta \sim 1$ after several tens of orbits. The transition radius moves out in time over $\sim 50 - 80$ orbits at the corresponding radius. Fig. 4 more clearly shows the difference between the resolved and unresolved cases (h01n256 and h02n256) by face-on and edge-on slices of density and plasma- β at a later stage of the evolution. When the thermal scale height is resolved, the disk is much thinner with scale height $H \sim H_{\text{th}}$, more dense, moderately magnetized with $\beta \sim 1$, and less turbulent in the midplane inside R_{circ} . The disk still maintains the diffuse, strongly magnetized ($\beta \ll 1$) state outside the midplane, which

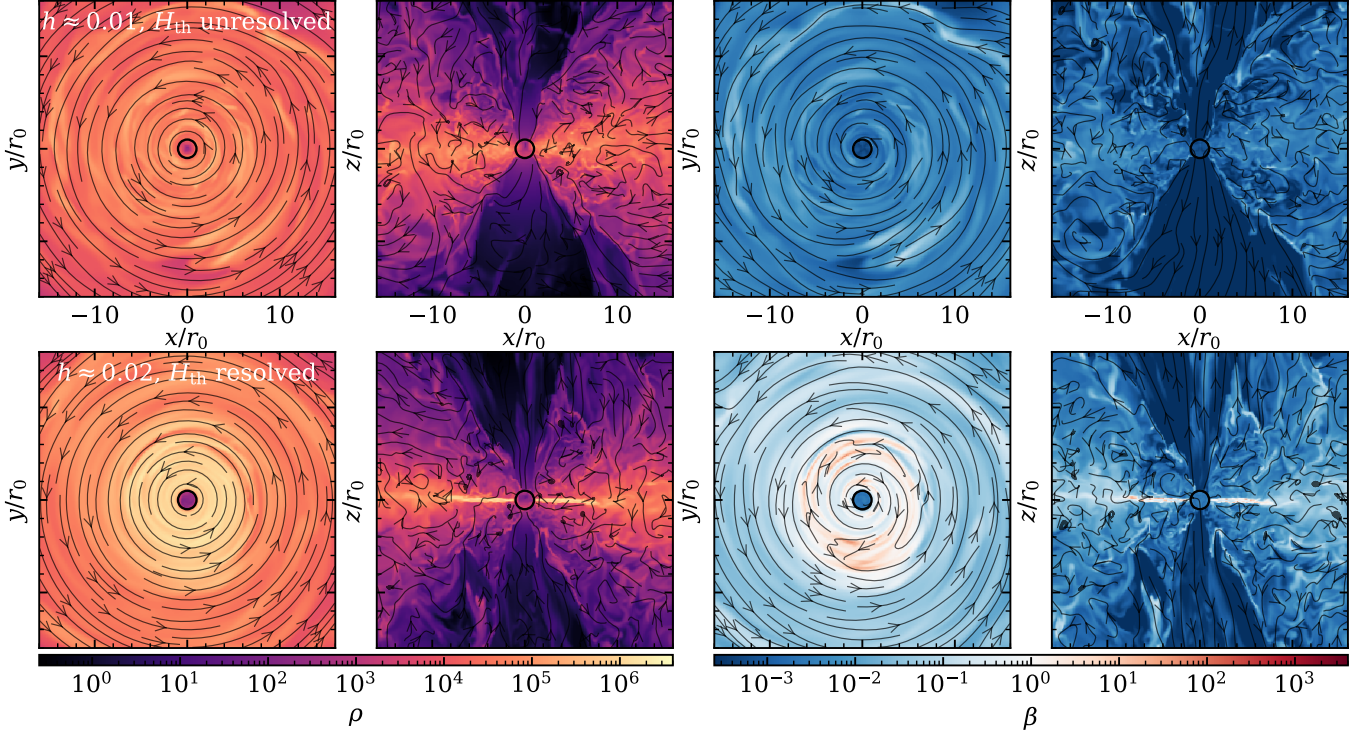


FIG. 4.— Face-on and edge-on slices of (left) density with velocity streamlines and (right) plasma- β with magnetic field lines at the end of the simulation. Top: a case with the thermal scale height ($h = 0.0125$, model h01n256 at $t/t_0 = 1.5 \times 10^4$) unresolved. Bottom: a case with the thermal scale height marginally resolved ($h = 0.025$, model h02n256 at $t/t_0 = 1.5 \times 10^4$). When H_{th} is unresolved, the disk is highly magnetized with $\beta \ll 1$. When H_{th} is resolved, the disk is still $\beta \ll 1$ outside the midplane, which is insensitive to resolution, but moderately magnetized close to the midplane with $\beta \sim 1$ inside R_{circ} .

is insensitive to resolution.

3.2. The structure of the accretion disk

Here we focus on the details of the structure and evolution of the accretion disk in the fiducial run (model h05n256, which has a thermal scale height that is small but resolved). Space-time diagrams of the azimuthally averaged midplane v_ϕ/v_K , β , and α for the fiducial run in Fig. 5 illustrate the basic evolution and properties of the system. The gas first inflows radially due to the lack of support from rotation and pressure. Soon the gas inflow forms a rotationally supported ($v_\phi \approx v_K$) disk for $R \lesssim 20r_0 \sim R_{\text{circ}}$ due to the initial angular momentum; the outer radius with significant angular momentum slowly moves to larger radii over time as gas is accreted to small radii in the disk, transferring its angular momentum to larger radii. The disk is initially rapidly accreting with $\alpha \gg 1$, strongly magnetized with $\beta \ll 1$, and vertically supported by the magnetic pressure, similar to the disks found in Gaburov et al. (2012), Hopkins et al. (2024a,b) and Guo et al. (2024). After $\sim 5000t_0$, it gradually collapses vertically to a $\beta \sim 1$ and $\alpha \sim 0.1$ state; this vertical collapse is shown as a function of time also in Fig. 8 below. This collapse proceeds inside out, occurring after a time of $\sim 50 - 80$ orbits at a given radius. Outside $\sim R_{\text{circ}}$, the gas still has midplane $\beta \ll 1$ at the end of the simulation. The magnetized disk at $\lesssim R_{\text{circ}}$ exhibits a quasi-steady state after reaching the $\beta \sim 1$ state. The flow at larger radii is presumably affected by the circularization process, so we suspect that radii $\lesssim R_{\text{circ}}$ are more representative of the “generic” toroidally dominated disk structure.

As shown in Fig. 6, the accretion rate grows quickly in the early stage and reaches a quasi-steady state after $2 \times 10^4 t_0$.

During the phase of rapidly increasing mass accretion rate the disk maintains $\alpha \gg 1$ and $\beta \ll 1$ while in the later stages when the mass accretion rate is only slowly increasing in time, the disk settles into the $\beta \sim 1$ state. Our qualitative interpretation of this result is that the magnetic flux is leaving the $\beta \ll 1$ disk due to buoyancy on a timescale of a few orbits (as shown in Fig. 11 below). When the mass accretion rate itself increases significantly over a few orbits, as it does at early times, the disk is able to maintain $\beta \ll 1$. But at later times when the accretion rate changes more slowly in time, the disk reaches its equilibrium quasi-steady structure with $\beta \sim 1$ and $\alpha \sim 0.1$. We also plot the accretion rate for other models with the same thermal scale height but different resolutions. Despite significant differences in disk geometry, the accretion rate as a function of both time and radius is very similar within a factor of ~ 2 .

The time and azimuthally averaged density, plasma- β , velocity streamlines, and magnetic field lines on different scales are shown in Fig. 7. A magnetized disk forms within $R \lesssim 50r_0$. The disk is rotationally supported within $R_{\text{edge}} \approx 40r_0$ (see Fig. 10 for a quantitative plot). The outer part of the disk ($R \gtrsim R_{\text{circ}}$) is strongly magnetized with $\beta \ll 1$. It transitions to a less magnetized disk with midplane $\beta \sim 1$ for $R \lesssim R_{\text{circ}}$, though keeps $\beta \ll 1$ outside the midplane. The gas inflows from large radii to the disk on small scales, with outflows in the polar region on large scales. The gas flows out in the $\beta \sim 1$ midplane on small scales. A spatially coherent mean radial magnetic field is generated by flux freezing in the inflow. The radial field finally transitions to a vertical field at small radii near the sink, and extends outward from two sides of the disk, forming large-scale loops. There is still zero net vertical flux.

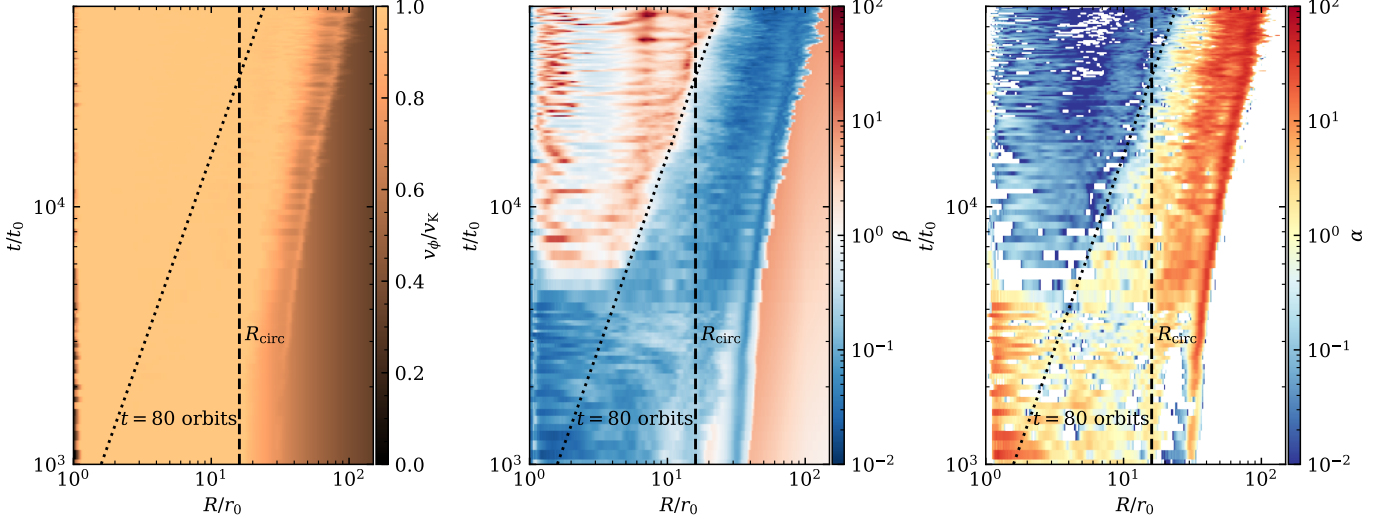


FIG. 5.— Space-time diagram of azimuthally averaged midplane v_ϕ/v_K (left), β (middle), and α (right) for the fiducial run (model h05n256). The black dashed lines mark the circularization radius $R_{\text{circ}} = 16 r_0$. The black dotted lines mark the time when the evolution time is 80 orbital periods at the corresponding radius. The gas first forms a strongly magnetized ($\beta \ll 1$), rapidly accreting ($\alpha \gg 1$), Keplerian ($v_\phi \approx v_K$) disk, then gradually collapses to a less magnetized ($\beta \sim 1$ and $\alpha \gtrsim 0.1$) state outwards over $\sim 50 - 80$ orbits. Outside $\sim R_{\text{circ}}$, the disk is still in the $\beta \ll 1$ and $\alpha \gg 1$ state.

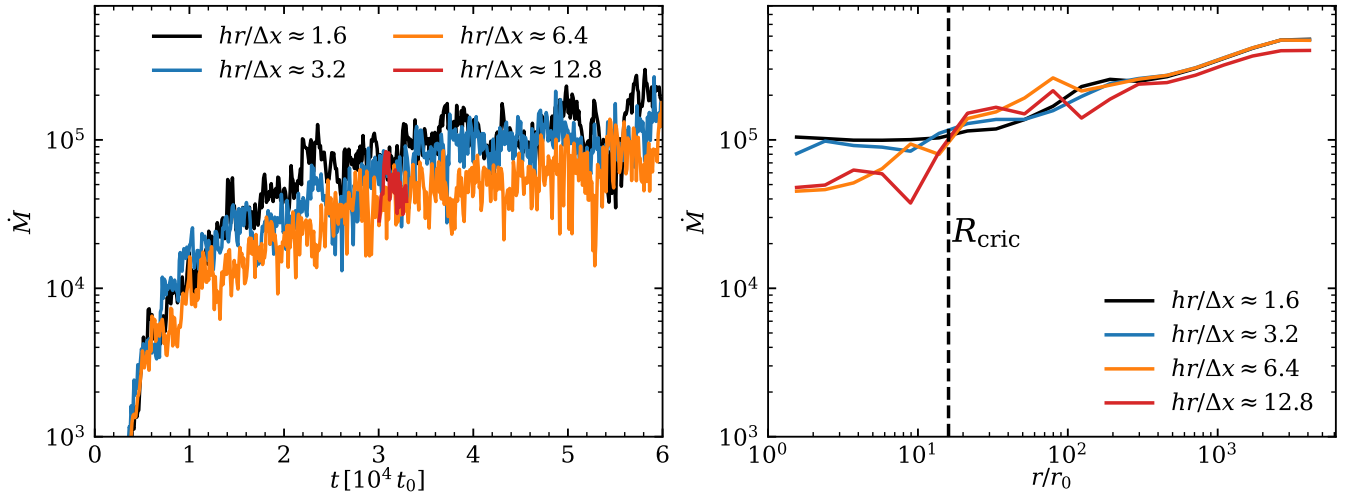


FIG. 6.— Left: accretion rate as a function of time for the run with the same thermal scale height ($h = 0.05$) but different resolutions (models h05n64, h05n128, h05n256, and h05n512t3). The dependence of the accretion rate on resolution is relatively weak, while the dependence of midplane gas pressure on resolution is strong (see Fig. 8). Right: accretion rate as a function of radius averaged over the end of the simulation ($3.1 \times 10^4 < t/t_0 < 3.3 \times 10^4$ for model h05n512t3 and $3 \times 10^4 < t/t_0 < 4 \times 10^4$ for others). The profile of mass accretion rate is overall flat, though it slightly increases with increasing radius since the simulation time is not much longer than the free-fall time at large radii ($\sim 10^3 r_0$).

Fig. 8 more quantitatively shows the time and azimuthally averaged vertical profiles of magnetic pressure compared with thermal pressure for models with the same thermal scale height ($h = 0.05$) but different resolutions (models h05n64, h05n128, h05n256, and h05n512t3). When the thermal scale height is unresolved (model h05n64 with $hr/\Delta x \sim 1.6$), the disk is highly magnetized everywhere with $P_{\text{gas}} \ll P_{\text{mag}}$ in the midplane. However, when the thermal scale height is resolved with $hr/\Delta x \gtrsim 3.2$, the disk is much less magnetized with $P_{\text{gas}} \sim P_{\text{mag}}$ ($\beta \sim 1$) in the midplane. When we further increase the resolution to $hr/\Delta x \sim 6.4$ or 12.8 , the profiles stay qualitatively similar with a slightly higher P_{gas} in the midplane. With increasing resolution, the magnetic pressure changes moderately, but the thermal pressure (and thus density since the disk is locally isothermal) in the midplane grows significantly as the thermal scale height transitions from

unresolved to resolved; at high resolution, the gas pressure approaches a Gaussian profile near the midplane, indicating a vertical equilibrium in which gravity is balanced by thermal pressure. Once the gas pressure is important near the midplane, the magnetic pressure has a small “dip” near the midplane. We note that, when the thermal scale height is not resolved, the gas pressure profile near the midplane (and hence density since the gas is locally isothermal) is closer to a power-law than Gaussian. These results are similar to the local shearing box simulations of Squire et al. (2024).

3.3. Collapse towards the midplane

We find that resolving or not resolving the gas thermal scale height changes the accretion flow structure and dynamics significantly. When the gas thermal scale height is resolved, the midplane is a gas-pressure-dominated thin disk with density

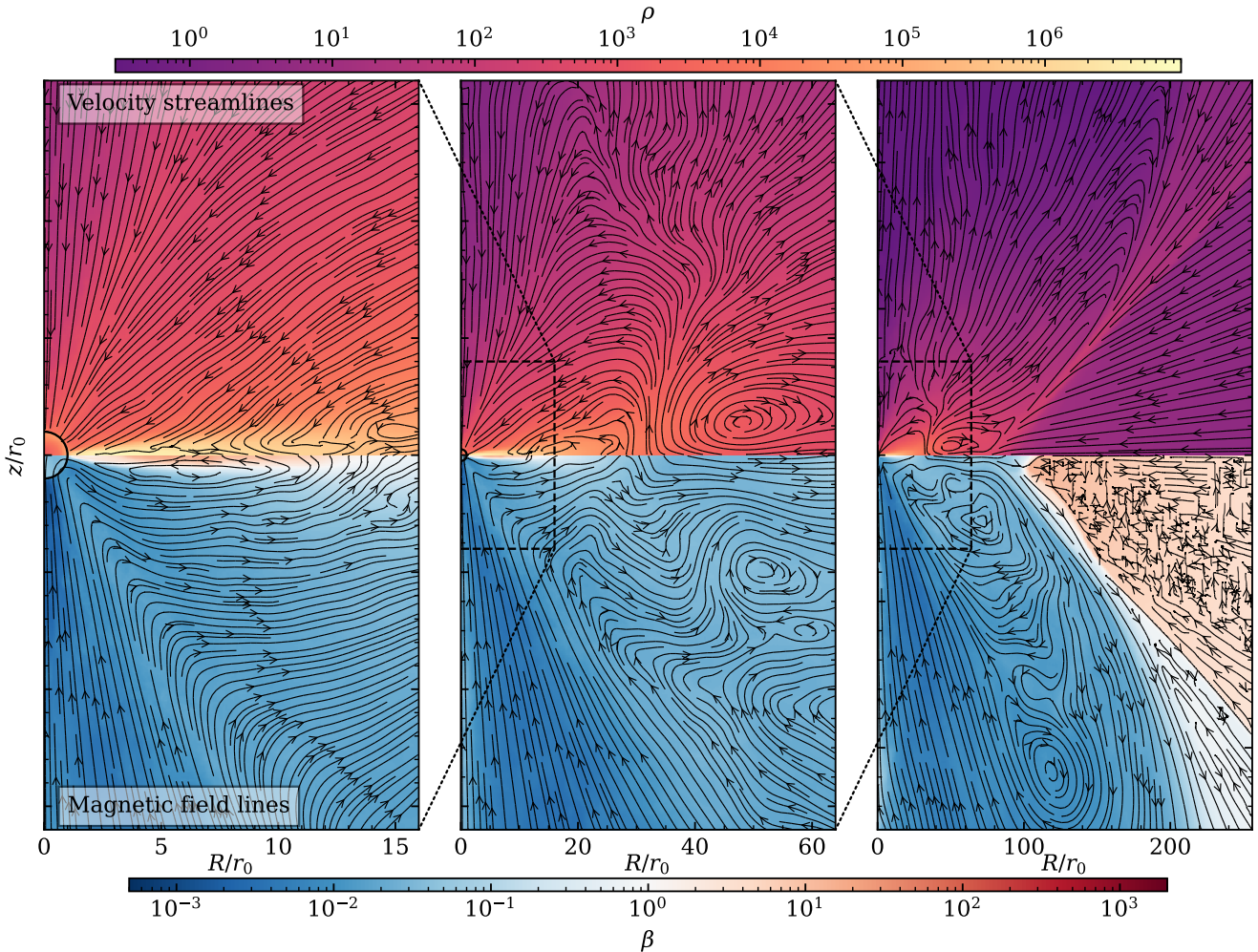


FIG. 7.— Time and azimuthally averaged images of density (upper) and plasma- β (lower) of the accretion disk from small (left) to large (right) scales for a model with the thermal scale height resolved (model h05n512t3 averaged over $3 \times 10^4 < t/t_0 < 3.3 \times 10^4$). The gas inflows from large scales to the disk on small scales with outflows in the polar region. A mean radial field was generated due to the inflow. The radial field finally transitions to a vertical field and extends outward from both sides of the disk, forming large-scale loops with zero net vertical flux. The disk is magnetized with midplane $\beta \sim 1$ and $\beta \ll 1$ everywhere outside the midplane.

scale height $H_\rho \sim H_{\text{th}}$, $\beta \sim \text{few}$, and $\alpha \sim 0.1$. When the gas thermal scale height is not resolved, the midplane remains magnetically supported with density scale height $H_\rho > H_{\text{th}}$, $\beta \ll 1$ and $\alpha \gg 1$. This strong dependence on the resolution relative to H_{th} is seen in Figs. 2, 3, 4, and 8.

Interestingly, however, the approach to a gas-pressure dominated midplane at high resolution occurs relatively slowly: the right panel of Fig. 8 shows the vertical profile of gas pressure and magnetic pressure at $R/r_0 = 10$ as a function of time from 10 orbits to 150 orbits. When the disk first forms, the midplane is magnetically dominated (see also Fig. 5) with $P_{\text{mag}} \gg P_{\text{gas}}$. It takes several tens of orbits for the gas to gradually collapse to the midplane and saturate to a state that is thermally dominated with $P_{\text{mag}} \sim P_{\text{gas}}$. This feature is also consistent with local shearing box simulations (Squire et al. 2024).

3.4. Turbulence and angular momentum transfer

To better diagnose the structure and angular momentum transfer of the accretion disk, we consider the stresses given

by

$$\boldsymbol{\Pi}_{\text{tot}} = \underbrace{\rho \mathbf{v} \mathbf{v}}_{\boldsymbol{\Pi}_{\text{kin}}} + \underbrace{P_{\text{gas}} \mathbf{I}}_{\boldsymbol{\Pi}_{\text{th}}} + \underbrace{\left(\underbrace{\frac{\mathbf{B} \cdot \mathbf{B}}{2} \mathbf{I}}_{\boldsymbol{\Pi}_{\text{pmag}}} - \underbrace{\mathbf{B} \mathbf{B}}_{\boldsymbol{\Pi}_{\text{tension}}} \right)}_{\boldsymbol{\Pi}_{\text{mag}}}. \quad (10)$$

The kinetic stresses can be further separated into $\boldsymbol{\Pi}_{\text{kin}} = \bar{\boldsymbol{\Pi}}_{\text{kin}} + \delta \boldsymbol{\Pi}_{\text{kin}}$ where the mean part $\bar{\boldsymbol{\Pi}}_{\text{kin}} = \rho \langle \mathbf{v} \rangle \langle \mathbf{v} \rangle$ with $\langle \cdot \rangle$ denoting time and angle average and the fluctuating part (the Reynolds stress) $\delta \boldsymbol{\Pi}_{\text{kin}} = \rho \delta \mathbf{v} \delta \mathbf{v}$ with the fluctuating velocities $\delta \mathbf{v} = \mathbf{v} - \langle \mathbf{v} \rangle$. Similarly, the magnetic (Maxwell) stresses $\boldsymbol{\Pi}_{\text{mag}} = \bar{\boldsymbol{\Pi}}_{\text{mag}} + \delta \boldsymbol{\Pi}_{\text{mag}}$ where $\bar{\boldsymbol{\Pi}}_{\text{mag}} = |\langle \mathbf{B} \rangle|^2 \mathbf{I}/2 - \langle \mathbf{B} \rangle \langle \mathbf{B} \rangle$ and $\delta \boldsymbol{\Pi}_{\text{mag}} = |\delta \mathbf{B}|^2 \mathbf{I}/2 - \delta \mathbf{B} \delta \mathbf{B}$ with fluctuating magnetic field $\delta \mathbf{B} = \mathbf{B} - \langle \mathbf{B} \rangle$. Then the α parameter is defined by

$$\alpha = \frac{\delta \boldsymbol{\Pi}_{\text{kin}}^{R\phi} + \delta \boldsymbol{\Pi}_{\text{mag}}^{R\phi} + \bar{\boldsymbol{\Pi}}_{\text{mag}}^{R\phi}}{\langle P_{\text{gas, midplane}} \rangle} \quad (11)$$

Fig. 9 plots the vertical profiles of time and azimuthally averaged α and its components: $\alpha \sim 0.1$ with the accretion

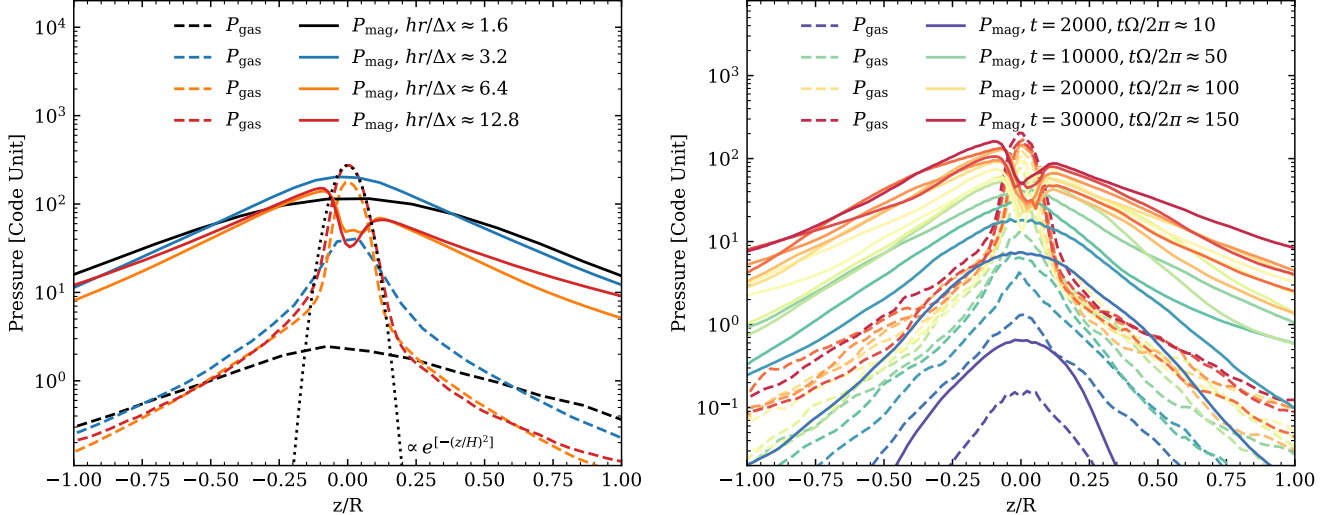


FIG. 8.— Left: vertical profile of time and azimuthally averaged magnetic and thermal pressures at $R/r_0 = 10$ for different resolutions, i.e., models h05n64, h05n128, h05n256, and h05n512t3. The profile is averaged over $3 \times 10^4 < t/t_0 < 3.3 \times 10^4$ for model h05n512t3 and $2.5 \times 10^4 < t/t_0 < 3.0 \times 10^4$ for others. The black dotted line shows a Gaussian profile with $H = \sqrt{2}hR$. The thermal pressure in the midplane $P_{\text{gas}} \ll P_{\text{mag}}$ for the case with lowest resolution of $hr/\Delta x \approx 1.6$ but $P_{\text{gas}} \sim P_{\text{mag}}$ otherwise. Right: vertical profile of azimuthally averaged magnetic and thermal pressures as a function of time, from blue to red in equal time increments of approximately 10 orbits at $R/r_0 = 10$ for the fiducial simulation (model h05n256). It takes several tens of orbits for the disk to collapse to the $\beta \sim 1$ state.

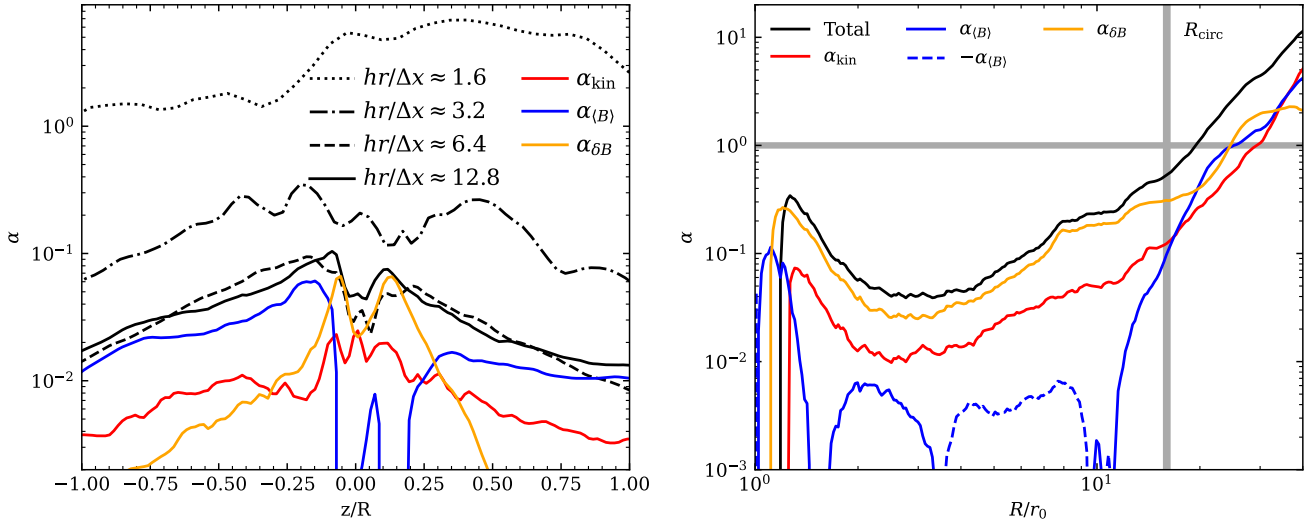


FIG. 9.— Left: vertical profile of time and azimuthally averaged α measured at $R/r_0 = 10$ for different resolutions (the same models as in Fig. 8) and its components for the highest resolution run. The disk is accreting efficiently with $\alpha \sim 0.1$. The accretion is dominated by the fluctuating Maxwell stresses in the midplane and by the mean stresses outside $|z/H_{\text{th}}| \gtrsim 2$. The parameter $\alpha \gtrsim 1$ if the thermal scale height is not resolved. Right: radial profiles of time and azimuthally averaged α ($|z/R| < 0.2$) and its three components for model h05n512t3. The disk shows $\alpha \sim 0.1$ with a weak dependence on radius inside R_{circ} . The turbulent magnetic part $\alpha_{\delta B}$ dominates the angular momentum transfer. Between R_{circ} and the outer edge of the disk R_{edge} , there is stronger angular momentum transfer with $\alpha \gtrsim 1$ dominated by both the mean stress $\alpha_{\langle B \rangle}$ and the fluctuating stress $\alpha_{\delta B}$.

driven by both the mean and the fluctuating magnetic stresses. The fluctuating magnetic stresses dominate in the midplane ($|z/R| < 0.1$), while the mean field dominates elsewhere. This is similar to the local shearing box simulations (Squire et al. 2024). The right panel of Fig. 9 plots the radial profile of α and its components for the model h05n512t3. On all scales within R_{circ} we find $\alpha \sim 0.1$ with a weak dependence on radius. Between R_{circ} and the outer edge of the disk $R_{\text{edge}} \approx 40 r_0$, there is stronger angular momentum transfer with $\alpha \sim 1$. It is dominated by both the mean field and the fluctuating field.

When the thermal scale height is not resolved, the turbulence

is much larger with $\alpha \gg 1$ (see Figs. 9); this is a consequence of similar magnetic field strengths but very different midplane gas densities and pressures in the two cases (H_{th} resolved and unresolved). In both the H_{th} resolved and unresolved regimes, however, the final mass accretion rate is quite similar within a factor of 2, as shown in Fig. 6 – this accretion rate is set by the free-fall rate of gas at large radii in our initial conditions. The resolved thermal scale height simulation has a smaller scale height and α at a given M relative to the unresolved thermal scale height simulation, leading to much higher midplane densities and pressures. We note that, the gas flows out for $|z| \lesssim H_{\text{th}}$ and most of the accretion happens

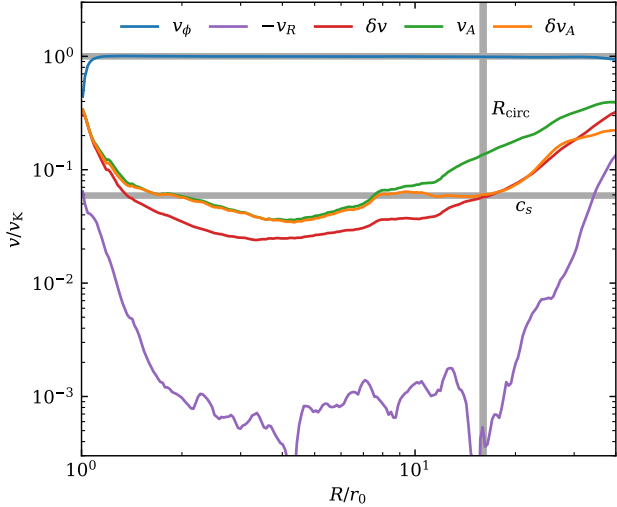


Fig. 10.— Radial profiles of time and azimuthally averaged rotational velocity, radial velocity, turbulent velocity, mean Alfvén velocity, and turbulent Alfvén velocity of the disk for $|z/R| < 0.2$ as a function of cylindrical radius for the model h05n512t3. The disk is rotationally supported within $\sim 40 r_0$. Radial advection is important outside R_{circ} with mean radial velocity $-v_R/v_K \sim 10^{-1}$. Within R_{circ} , the turbulence is transonic and trans-Alfvénic with $\delta v \sim \delta v_A \sim v_A \sim c_s$.

outside the midplane ($|z| \gtrsim H_{\text{th}}$), as shown in Fig. 7.

Fig. 10 compares the mass-weighted, time and azimuthally averaged mean and fluctuating velocities in the midplane as a function of radius. The turbulence within R_{circ} is essentially transonic and trans-Alfvénic with $\delta v^2 \sim \delta v_A^2 \sim v_A^2 \sim c_s^2$. The turbulence is likely driven by a combination of the MRI and Parker instability (Johansen & Levin 2008; Pessah & Psaltis 2005; Squire et al. 2024). The radial velocity is $-v_R/v_K \sim 10^{-3}$ within R_{circ} but larger with $-v_R/v_K \sim 10^{-1}$ outside R_{circ} , indicating the relative importance of radial advection on larger scales.

3.5. Sustaining the magnetic field

Squire et al. (2024) performed a detailed analysis of the dynamo in their local shearing box simulations of disks with strong toroidal fields. The results demonstrated that the net azimuthal field is sustained by a dynamo mechanism. In the shearing box, vertical turbulent diffusion and vertical outflows continuously remove azimuthal flux out of the top and bottom boundaries of the simulation. This loss is balanced by creation of azimuthal flux via shearing of the radial field. Squire et al. (2024)'s analysis of the origin of the radial field from this azimuthal flux was somewhat inconclusive and more work to understand this aspect of the dynamo is needed. Here we focus primarily on global effects not present in the shearing box, in particular the role of radial gas flow in advecting magnetic field in from larger radii.

A spatial and time average of the induction equation 4 yields

$$\frac{\partial \langle \mathbf{B} \rangle}{\partial t} = \nabla \times (\langle \mathbf{v} \rangle \times \langle \mathbf{B} \rangle) + \nabla \times \delta \mathcal{E}, \quad (12)$$

where $\langle \mathbf{v} \rangle$ is the time and azimuthally averaged mean flow, $\langle \mathbf{B} \rangle$ is the mean magnetic field, and the turbulent *electromotive force* (EMF) $\delta \mathcal{E} = \langle \delta \mathbf{v} \times \delta \mathbf{B} \rangle$, which is responsible for dynamo action, is nonzero due to the correlation between $\delta \mathbf{v}$ and $\delta \mathbf{B}$.

We rewrite the induction equation as (note that $\nabla \cdot \mathbf{B} = 0$)

$$\frac{\partial \langle \mathbf{B} \rangle}{\partial t} = \underbrace{-\langle \mathbf{v} \rangle \cdot \nabla \langle \mathbf{B} \rangle}_{\text{advection}} - \underbrace{\langle \mathbf{B} \rangle \nabla \cdot \langle \mathbf{v} \rangle}_{\text{compression}} + \underbrace{\langle \mathbf{B} \rangle \cdot \nabla \langle \mathbf{v} \rangle}_{\text{stretching}} + \underbrace{\nabla \times \delta \mathcal{E}}_{\text{turbulence}}, \quad (13)$$

to show the advection (including compression as the flow is fully compressive), stretching, and turbulence terms. For the azimuthal field B_ϕ , Eq. 13 becomes

$$\begin{aligned} \frac{\partial \langle B_\phi \rangle}{\partial t} = & -\underbrace{(\langle v_R \rangle \partial_R \langle B_\phi \rangle + \langle v_\phi \rangle \langle B_R \rangle / R + \langle B_\phi \rangle \partial_R \langle v_R \rangle)}_{\text{radial advection}} \\ & - \underbrace{(\langle B_\phi \rangle \partial_z \langle v_z \rangle + \langle v_z \rangle \partial_z \langle B_\phi \rangle)}_{\text{vertical advection}} \\ & + \underbrace{(\langle B_R \rangle \partial_R \langle v_\phi \rangle + \langle B_z \rangle \partial_z \langle v_\phi \rangle)}_{\text{stretching}} \\ & + \underbrace{\partial_z \delta \mathcal{E}_R - \partial_R \delta \mathcal{E}_z}_{\text{turbulence}}, \end{aligned} \quad (14)$$

including contributions from radial advection, vertical advection, stretching, and turbulence.

In Fig. 11, we analyze the time and azimuthally averaged contribution of each component in Eq. 14 for toroidal field $\langle B_\phi \rangle$ at $R/r_0 = 10$ and $R/r_0 = 30$ over the quasi-steady state ($3 \times 10^4 < t/t_0 < 6 \times 10^4$, that is, from 150 to 300 orbits at $R/r_0 = 10$). We normalize each term by $\langle B_\phi \rangle \Omega_{\text{Kep}}(R)/(2\pi)$ such that a value of 1 implies that the particular term would grow or decay $\langle B_\phi \rangle$ at a given z by 100% over one orbit. For comparison, we show the evolution of the vertical profile of B_ϕ and $\sqrt{2P_{\text{gas}}}$ at $R/r_0 = 10$ and $R/r_0 = 30$ in the top panels of Fig. 11. The azimuthal field B_ϕ at $R = 10 r_0$ gradually increases, flips its sign after ~ 100 orbits, and saturates with $B_\phi \sim -\sqrt{2P_{\text{gas}}}$. The system is in a statistically steady state, though the flip of sign at $R = 10 r_0$ complicates interpreting the time-averaged dynamo contributions to the evolution of the field. As we noted previously, the disk at $R = 30 r_0$ is still radially supported by rotation but is vertically supported by magnetic pressure with a much smaller $\beta \ll 1$ and $\alpha \gg 1$ during the simulation.

At shown in Fig. 11 (bottom left), at $R = 10 r_0$, the azimuthal magnetic field is continuously regenerated and escaping the disk. Similar to the local simulations (Squire et al. 2024), fields are replenished and expelled over several orbit timescales, with strong flux creation by shearing of radial field (dominated by the term $\langle B_R \rangle \partial_R \langle v_\phi \rangle$) balanced by its diffusion via turbulence (dominated by $\partial_z \delta \mathcal{E}_R$). The vertical advection of the azimuthal field is subdominant with its two subterms $-\langle B_\phi \rangle \partial_z \langle v_z \rangle / (\langle B_\phi \rangle \Omega_{\text{Kep}}/(2\pi)) \sim 0.3$ and $-\langle v_z \rangle \partial_z \langle B_\phi \rangle / (\langle B_\phi \rangle \Omega_{\text{Kep}}/(2\pi)) \sim -0.3$ canceling each other out. The radial advection of the azimuthal field is approximately zero, making it approximately equivalent to the shearing box. Though not shown in the figure, the first two subterms $-\langle v_\phi \rangle \langle B_R \rangle / R / (\langle B_\phi \rangle \Omega_{\text{Kep}}/(2\pi)) \sim 0.5$ and $-\langle B_\phi \rangle \partial_R \langle v_R \rangle / (\langle B_\phi \rangle \Omega_{\text{Kep}}/(2\pi)) \sim -0.5$ are relatively large but cancel out each other while the third term $-\langle v_R \rangle \partial_R \langle B_\phi \rangle / (\langle B_\phi \rangle \Omega_{\text{Kep}}/(2\pi)) \sim 0$ is negligible.

Fig. 11 (bottom right) shows the same analysis for the disk

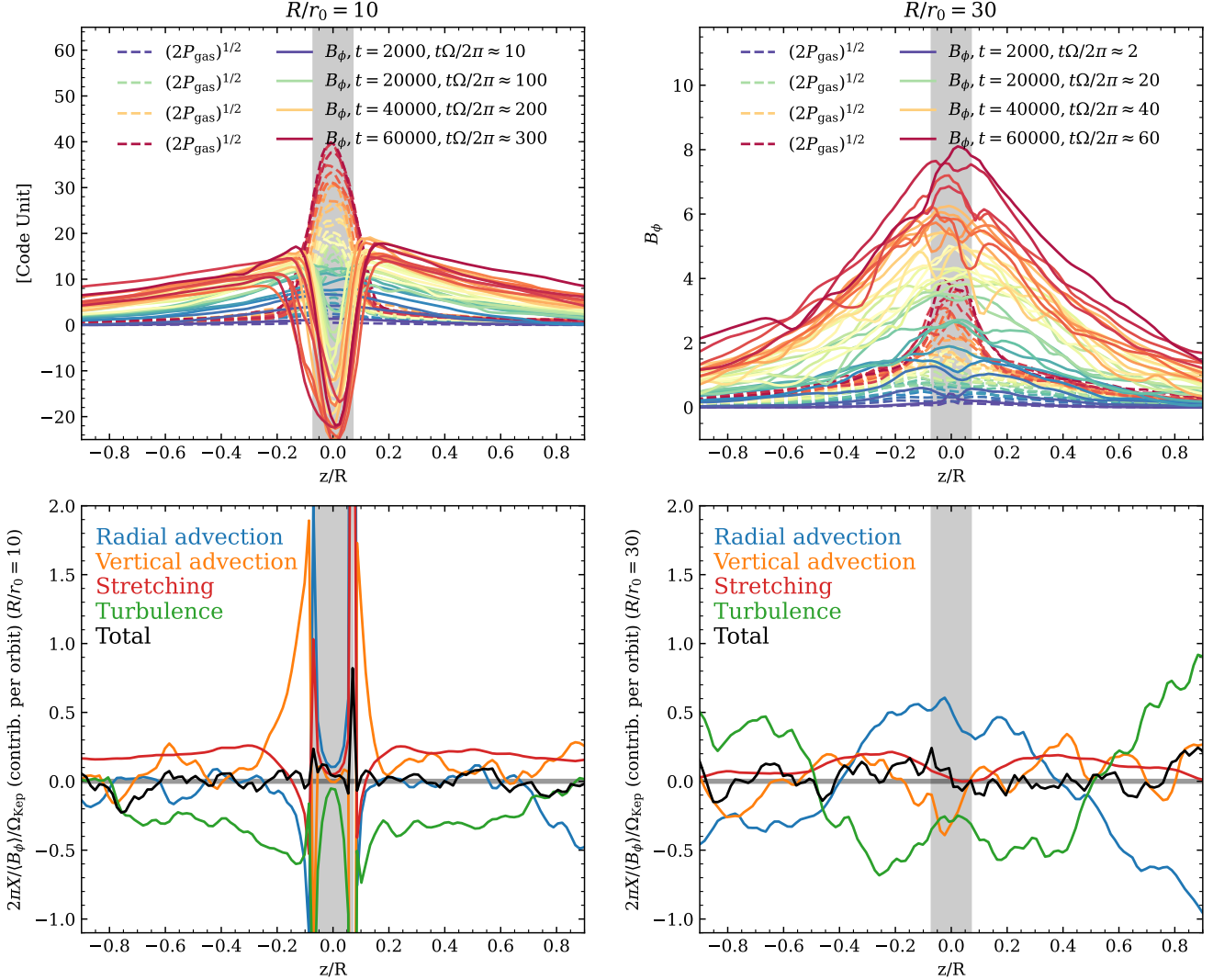


FIG. 11.— Top: vertical profile of azimuthal magnetic field B_ϕ and $(2P_{\text{gas}})^{1/2}$ for comparison as a function of time, from blue to red in equal time increments of $2000 t_0$ at $R/r_0 = 10$ (left) and 30 (right). Bottom: contribution of the terms in the induction equations Eq. 14 averaged over $3 \times 10^4 < t/t_0 < 6 \times 10^4$. Total includes all the terms on the right-hand side of the averaged induction equation. Each term is normalized by $\langle B_\phi \rangle \Omega_{\text{Kep}}(R) / (2\pi)$ such that a value of 1 implies that the particular term would grow or decay $\langle B_\phi \rangle$ at a given z by 100% over one orbit. At $R/r_0 = 10$ where midplane $\beta \sim 1$ and the field flips, the fields are replenished and expelled over several orbit timescales, with strong flux creation by shearing of radial field balanced by its diffusion via turbulence. The radial advection and compression are less important. At $R/r_0 = 30$ where $\beta \ll 1$, the radial advection of the field B_ϕ replenishes the field in the midplane quickly.

at $R = 30 r_0 > R_{\text{circ}}$. As in our analysis at $R = 10 r_0$, the fields are still replenished by shearing of the radial magnetic field and expelled by turbulent diffusion. Nonetheless, the radial advection of the field B_ϕ (dominated by the term $-\langle B_\phi \rangle \partial_R \langle v_R \rangle$) replenishes the field quickly due to the relatively large radial velocity $-\langle v_R \rangle / v_K \sim 0.1$. This may explain why the disk is able to maintain a $\beta \ll 1$ state at larger radii. The fact that radial advection is only important exterior to the circularization radius implies that, at least in the simulations carried out here, radial advection of the magnetic field is important in setting the magnetic field structure at large radii but not in the bulk of the disk.

For the mean radial field $\langle B_R \rangle$, we have shown in Fig. 7 that it is generated from the large-scale inflow of the gas. The large-scale inflow forms large-scale poloidal loops from the initially toroidal magnetic field, which leads to both mean radial and mean vertical magnetic field on smaller scales. Note, though, that the system still has zero net vertical flux since the mean vertical field is symmetric about the midplane.

3.6. Robustness of the $\beta \sim 1$ disk

To investigate the robustness of the $\beta \sim 1$ disk and its dependence on various factors, including the strength of the magnetic field, vertical magnetic field, and numerical method, we perform miscellaneous tests here.

Strength of the initial magnetic field— First, we vary the strength of the initial magnetic field to examine the robustness of the $\beta \sim 1$ disk. We run a case (model h05b10) similar to the fiducial run except with a stronger initial magnetic field (lower $\beta = 1/10$). The space-time diagram of midplane β is shown in Fig. 12. Despite a ten times stronger initial magnetic field, the system still collapses to a $\beta \sim 1$ disk within ~ 80 orbits, a timescale similar to the fiducial run. Therefore the $\beta \sim 1$ state does not depend on the initial strength of the large-scale magnetic field as long as the initial magnetic field is strong enough to form the $\beta \sim 1$ state during the circularization of the disk.

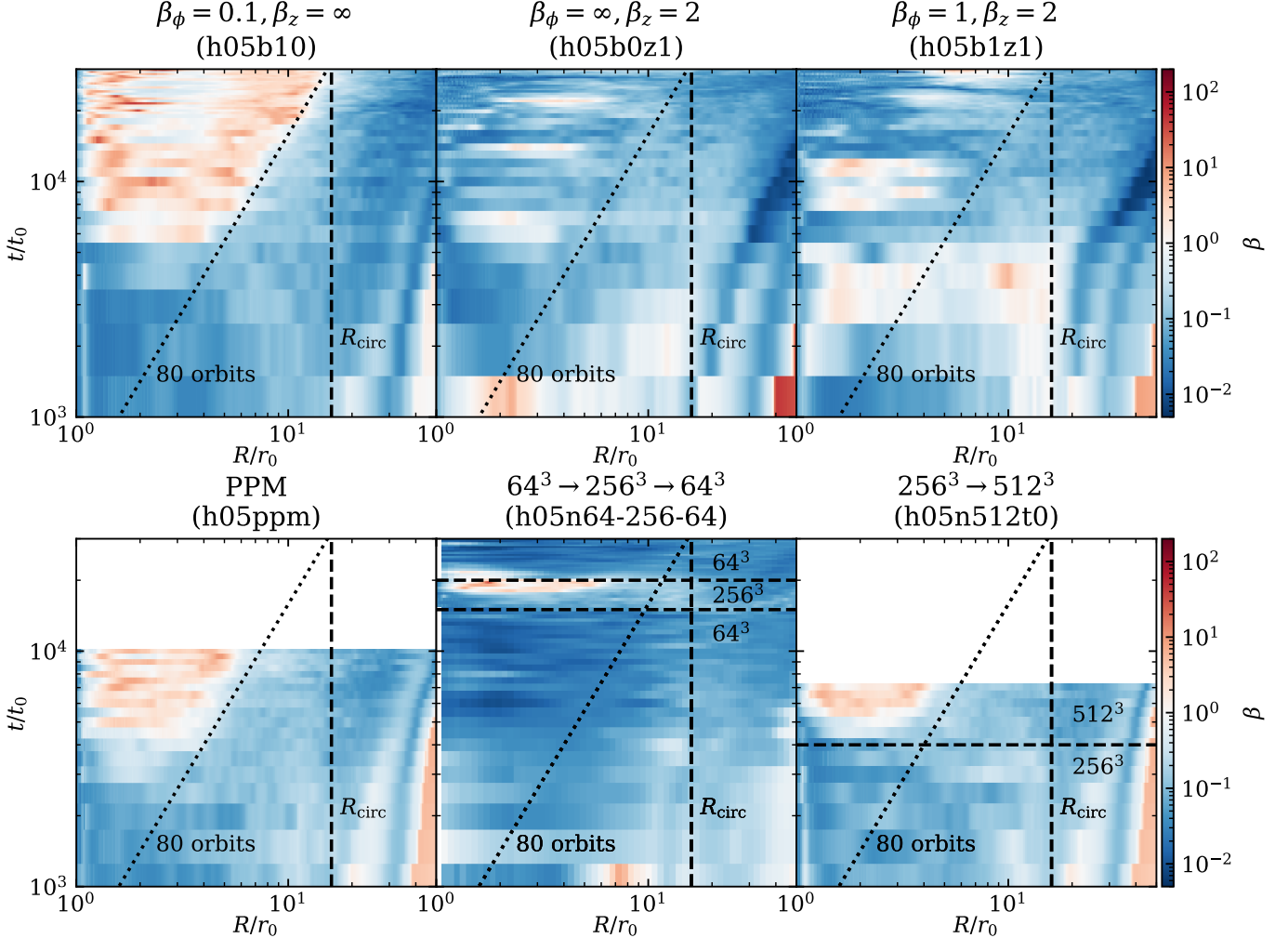


FIG. 12.— Space-time diagram of azimuthally averaged midplane β , similar to Fig. 3, but for miscellaneous tests. Top left: stronger initial magnetic field strength shows a similar transition to the $\beta \sim 1$ disk within $\sim R_{\text{circ}}$ over ~ 80 orbits. Top center: disk with initially purely vertical magnetic field sustains a strongly magnetized ($\beta < 1$) state. Top right: disk with both toroidal and vertical field shows a similar strongly magnetized ($\beta < 1$) state. Bottom left: higher-order PPM reconstruction method confirms the disk state transition similar to the model using PLM. Bottom center: the initially H_{th} -unresolved disk gradually collapses to $\beta \sim 1$ after two levels of mesh refinement and returns to $\beta \ll 1$ after derefinement. Bottom right: the initial collapse around $\sim 5 \times 10^3 t_0$ in the fiducial run is reproduced in a higher resolution run restarted at $4 \times 10^3 t_0$.

Net vertical magnetic field— As found by many previous studies (Hawley et al. 1995; Bai & Stone 2013; Salvesen et al. 2016; Zhu & Stone 2018), including a net vertical magnetic field can help sustain a strongly magnetized ($\beta < 1$) disk midplane. Here we perform a simulation with a purely vertical magnetic field with strength $\beta_z = P_{\text{gas}}/(B_z^2/2) = 2$ (model h05b0z1). The results are shown in Fig. 12. Consistent with previous studies, the system reaches a $\beta \lesssim 1$ state with a larger density scale height. We also see the polarity flips of B_ϕ near the midplane and a similar structure of v_R and B_R , as shown in Fig. 13. The stress is dominated by the mean component of the Maxwell stress, $\alpha_{\langle B \rangle}$. Therefore, it is a rather different mode of accretion compared with the ZNVF cases, but consistent with the large-scale channel mode with vertical flux (e.g., Zhu & Stone 2018). We also run a case (model h05b1z1) with both the toroidal and vertical field for completeness and show the results in Fig. 12. The final magnetization of the disk is qualitatively similar to the case with purely vertical fields. Therefore, similar to previous studies, the accretion with vertical field shows qualitatively different accretion properties from ZNVF cases.

Reconstruction method— Most of the runs are performed using the PLM reconstruction method. Here we rerun the fiducial case but with the PPM reconstruction method (h05ppm) for $t/t_0 = 10^4$ to test the robustness of the results against the numerical method. The space-time diagram shown in Fig. 12 shows a similar transition from $\beta \ll 1$ to $\beta \sim 1$ state, indicating that the results are very similar to the fiducial run.

Mesh refinement and derefinement— To further confirm that the transition of magnetic state is due to numerical resolution, we refine the mesh of the model h05n64 at $t/t_0 = 1.5 \times 10^4$ by a factor of 4, and run it for $5 \times 10^3 t_0$ (model h05n64-256). Then we derefine the mesh back to the original resolution and run it for $10^4 t_0$ (model h05n64-256-64). As shown in Fig. 12, the disk gradually collapses after several to tens of orbits with midplane plasma- β gradually increasing to $\beta \sim 1$ after refinement and returning to $\beta \ll 1$ after derefinement. Therefore the $\beta \sim 1$ state is clearly dependent on resolution. We do not find such a transition if we only refine the mesh of the model h05n64 by a factor of 2, implying that the dependence of the transition on resolution may not be very sharp. We also

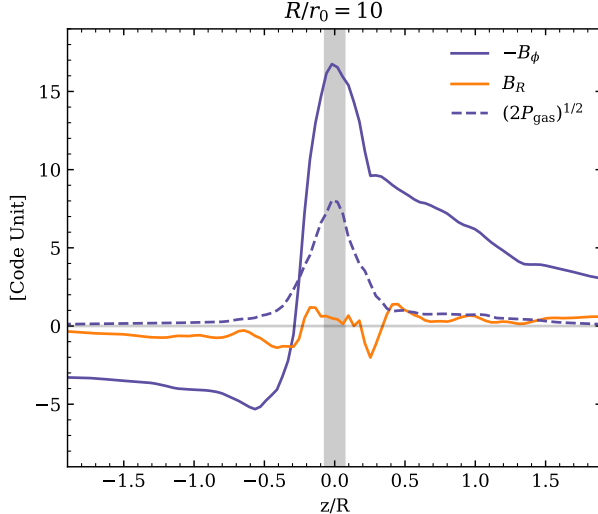


FIG. 13.— Vertical profile of azimuthally averaged B_ϕ , B_R , and $(2P_{\text{gas}})^{1/2}$ at $R/r_0 = 10$ for the model initialized with vertical magnetic field (model h05b0z1) at the end of the simulation ($t/t_0 = 3 \times 10^4$). The magnetic field dominates the midplane with a polarity flip near the midplane.

restart the fiducial run at $4000 t_0$, refine it by a factor of 2, and run it for $3000 t_0$ (model h05n512t0) to capture the initial collapse process in the fiducial run with a higher resolution. As shown in Fig. 12, the collapse process of the disk is very similar to the fiducial case.

To summarize: The $\beta \sim 1$ disk is robust against various parameters. Varying thermal scale height, initial toroidal magnetic field strength, and numerical method give qualitatively similar $\beta \sim 1$ disks within $\sim R_{\text{circ}}$. A vertical field helps to sustain a different disk state with a larger saturated magnetic flux characterized by $\beta \lesssim 1$. Further tests with smaller H_{th} would be particularly useful, but would require significantly higher resolution.

4. SUMMARY AND DISCUSSION

We have presented and characterized three-dimensional idealized global MHD simulations of a strongly magnetized accretion disk dominated by toroidal magnetic fields. Our equation of state fixes the temperature via a specified value of the disk aspect ratio (i.e., H/R assuming gas pressure support). The disk forms by gas inflow and circularization from uniform cold gas with a toroidal magnetic field. We find that the system maintains a strong mean azimuthal field in the midplane, with $\beta \sim 1$, trans-Alfvénic fluctuations and large accretion stresses $\alpha \sim 0.1$. The disk is turbulent with $\delta v^2 \sim \delta v_A^2 \sim v_A^2 \sim c_s^2$, likely driven by a combination of MRI and Parker instabilities (Balbus & Hawley 1992; Kim & Ostriker 2000; Pessah & Psaltis 2005; Johansen & Levin 2008; Das et al. 2018; Squire et al. 2024). Outside the midplane, the disk is strongly magnetized with $\beta \ll 1$. A net vertical flux, which is traditionally thought to be necessary to sustain such strong magnetization ($\beta \sim 1$ in the midplane) and large α , is not in fact required. That being said, we find that the addition of vertical magnetic flux can generate even stronger magnetization, as illustrated by previous works (Bai & Stone 2013; Salvesen et al. 2016; Zhu & Stone 2018).

We show explicitly that the azimuthal field in the disk is continuously escaping along the vertical direction but is also replenished via a local dynamo. In the bulk of the disk interior to the circularization radius, radial advection of azimuthal

magnetic field from larger radii is subdominant in sustaining the $\beta \sim 1$ state and the toroidal field (though it is important exterior to the circularization radius where the gas inflows more rapidly). In this sense shearing box simulations should be a reasonable approximation to the disk dynamics found here. Indeed our global results are broadly similar to the “low- β state” zero-net-vertical-flux shearing box results of Squire et al. (2024).

We find that the gas first forms a highly magnetized ($\beta \ll 1$) Keplerian disk, but then gradually collapses to a moderately magnetized ($\beta \sim 1$) state from the inside out over $\sim 50 - 80$ orbits (Fig. 8). The disk also can be strongly magnetized with $\beta \ll 1$ and $\alpha \gg 1$ when the thermal scale height is not resolved (Figs. 2, 3, 4, and 9.). However, when we resolve the thermal scale height with $\gtrsim 4$ cells, the disk slowly collapses to a disk with $\beta \sim 1$ in the midplane over $\sim 50 - 80$ orbits at the corresponding radius; the disk remains magnetically dominated with $\beta \ll 1$ well off the midplane.

The disk properties presented here bear some similarities to the strongly magnetized accretion disks found in related global simulations by Gaburov et al. (2012), Hopkins et al. (2024a,b) and Guo et al. (2024). Gaburov et al. (2012) found the formation of a toroidally dominated $\beta \sim 0.1$ disk in simulations of accretion disks formed by molecular cloud disruption in galactic nuclei. Hopkins et al. (2024a,b) performed simulations following the accretion flow onto a supermassive black hole (SMBH) in cosmological simulations from \sim Mpc scales and found a disk that is highly magnetized ($\beta \sim 10^{-4}$), toroidal field-dominated, vertically supported by the strong magnetic pressure, with $\alpha \gg 1$ due to the strong magnetic stress. Hopkins et al. (2025) re-ran a new case with a higher temperature floor of 10^6 K (see their Fig. 31) so that thermal scale height is resolved; they still found a strongly magnetized state with $\beta \ll 1$ after ~ 50 orbits at inner boundary. Guo et al. (2024) found similar strongly-magnetized disks with $\beta \sim 10^{-3}$ when following the fueling of SMBH in elliptical galaxies from a turbulent cooling medium on galactic scales.

Overall, our idealized simulations capture a number of these features, such as the dominant toroidal field and trans-Alfvénic fluctuations. Most importantly, our results show that the magnetic flux does not immediately escape vertically, as previously argued from both local and global simulations (Salvesen et al. 2016; Fragile & Sadowski 2017); rather, the disk can sustain a $\beta \sim 1$ field against rapid escape via a dynamo mechanism. However, a critical difference is that the midplane β in our simulations is markedly higher than the solutions in Hopkins et al. (2024b) and Guo et al. (2024), with $\beta \sim 1$ instead of $\beta \ll 1$. As in the local shearing box simulations of Squire et al. (2024), the only situation in which we sustain $\beta \ll 1$ in the bulk of the disk for the full duration of our global simulations is when the midplane thermal scale height of the gas is poorly resolved (Fig. 8). The similarity of our global simulations to shearing box simulations in this respect shows that radial advection of magnetic flux does not appear to generically maintain a $\beta \ll 1$ toroidal field given such a state at larger radii.

The difference between our global simulations and those of Hopkins et al. (2024b) and Guo et al. (2024) remains unclear. It may be that the latter are simply not well enough resolved – this could reconcile the differences – or it could be that the more complex gas thermodynamics and gas inflow properties including strong asymmetry, warps, and more turbulence in the more realistic global models change the efficiency of maintaining the $\beta \ll 1$ state. It is striking that our global

simulations maintain $\beta \ll 1$ and $\alpha \gg 1$ for dozens of dynamical times (orbits) in the earlier phase when the accretion rate is increasingly rapidly in time so that the ambient disk conditions are evolving on the timescale that magnetic flux is escaping (Figs. 5 and 6). The simulations also maintain $\alpha \gtrsim 1$ somewhat exterior to the circularization radius (but still in the rotationally dominated part of the flow). These may be clues regarding conditions under which disks can maintain $\beta \ll 1$. More work on understanding this aspect of our simulations and the connection to the related global simulations of Hopkins et al. (2024b); Guo et al. (2024) is clearly needed.

The strong toroidal magnetic field state found in Squire et al. (2024) and here may naturally explain the efficiency of angular momentum transport $\alpha \sim 0.1 - 0.4$ estimated in dwarf novae and X-ray transient outbursts (King et al. 2007; Tetarenko et al. 2018). While the inclusion of other physics can do so as well (e.g., Hirose et al. 2014; Begelman et al. 2015; Scepi et al. 2018), the strong toroidal field disks studied in Squire et al. (2024) and here appear to produce $\alpha \sim 0.1 - 0.5$ relatively independent of other aspects of the simulation.

It is not clear if the results presented here are fully converged. Local simulations in Squire et al. (2024) suggest that the midplane β and α are non-monotonic with resolution (see their Fig. 17). With resolution increasing, the disk transport level first suddenly decreases from $\alpha \sim 1$ to $\alpha \sim 0.1$ then gradually increases with increasing resolution to $\alpha \simeq 0.5$ at the highest resolution studied. A resolution of at least 10 cells per thermal scale height is required to approach convergence in the local shearing box simulations; this is a resolution ~ 2 times better than the fiducial case here in which case it is possible that we actually underestimate the saturated magnetic field strength and α by a modest amount. Our global simulations also have limited dynamic range between the circularization radius and inner radius, and between the disk scale height and local disk radius. Further simulations with larger separation between R_{circ} and r_{in} , smaller thermal scale height, and higher resolution would be valuable.

We thank Yuri Levin for useful conversations. We acknowledge the EuroHPC Joint Undertaking for awarding this project access to the EuroHPC supercomputer LUMI, hosted by CSC (Finland) and the LUMI consortium through a EuroHPC Regular Access call. The authors are pleased to acknowledge that the work reported on in this paper was substantially performed using the Princeton Research Computing resources at Princeton University, which is consortium of groups led

by the Princeton Institute for Computational Science and Engineering (PICSciE) and Office of Information Technology’s Research Computing. This work was supported in part by NSF AST grant 2107872, by a Simons Investigator grant to EQ, and by a grant from the Simons Foundation (888968, E.C. Ostriker, Princeton University PI) as part of the Learning the Universe Collaboration. JS acknowledges the support of the Royal Society Te Apārangi, through Marsden-Fund grant MFP-UOO2221 and Rutherford Discovery Fellowship RDF-U001804. This work benefited from EQ’s and JS’s stays at the Kavli Institute for Theoretical Physics, supported by NSF PHY-2309135.

Software: AthenaK (Stone et al. 2024)

APPENDIX

RESOLUTION OF THE SIMULATIONS

For clarity, Fig. 14 illustrates the resolution of the highest resolution run (model h05n512t3 and h05n512t1). The resolution for other simulations is changed everywhere accordingly. The resolution is roughly uniform logarithmically. The highest resolution covers a region of $r \lesssim 10 r_0$.

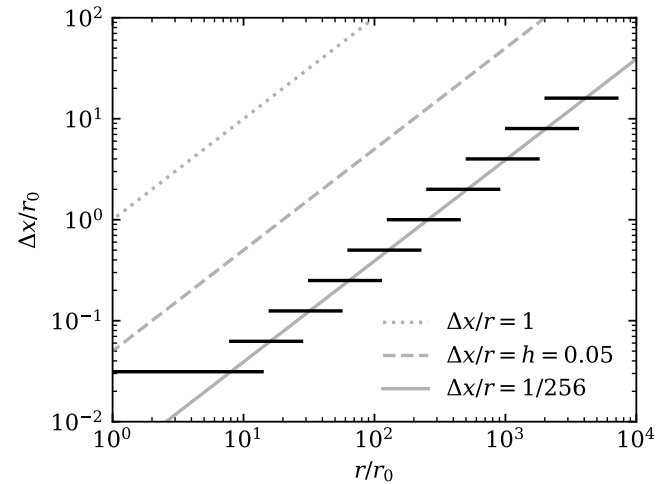


FIG. 14.— Size of cells (black) as a function of spherical radius in the highest resolution run. The overlap of the black lines is from the conversion from Cartesian to spherical coordinates. Gray lines mark characteristic resolution of $\Delta x/r = 1$, 0.05, and $1/256$. The resolution for other runs is adjusted everywhere accordingly.

REFERENCES

Bai X.-N., Stone J. M., 2013, *ApJ*, **767**, 30
 Balbus S. A., Hawley J. F., 1991, *ApJ*, **376**, 214
 Balbus S. A., Hawley J. F., 1992, *ApJ*, **400**, 610
 Begelman M. C., Pringle J. E., 2007, *MNRAS*, **375**, 1070
 Begelman M. C., Armitage P. J., Reynolds C. S., 2015, *ApJ*, **809**, 118
 Blandford R. D., Payne D. G., 1982, *MNRAS*, **199**, 883
 Das U., Begelman M. C., Lesur G., 2018, *MNRAS*, **473**, 2791
 Fragile P. C., Sadowski A., 2017, *MNRAS*, **467**, 1838
 Frank J., King Å., Raine D. J., 2002, *Accretion Power in Astrophysics*: Third Edition
 Gaburov E., Johansen A., Levin Y., 2012, *ApJ*, **758**, 103
 Goodman J., 2003, *MNRAS*, **339**, 937
 Guo M., Stone J. M., Quataert E., Kim C.-G., 2024, *arXiv e-prints*, p. arXiv:2405.11711
 Hawley J. F., Gammie C. F., Balbus S. A., 1995, *ApJ*, **440**, 742
 Hirose S., Blaes O., Krolik J. H., Coleman M. S. B., Sano T., 2014, *ApJ*, **787**, 1
 Hopkins P. F., et al., 2024a, *The Open Journal of Astrophysics*, **7**, 18
 Hopkins P. F., et al., 2024b, *The Open Journal of Astrophysics*, **7**, 19
 Hopkins P. F., et al., 2025, *The Open Journal of Astrophysics*, **8**, 48
 Jiang Y.-F., Blaes O., Kaul I., Zhang L., 2025, *arXiv e-prints*, p. arXiv:2505.09671
 Johansen A., Levin Y., 2008, *A&A*, **490**, 501
 Kim W.-T., Ostriker E. C., 2000, *ApJ*, **540**, 372
 King A. R., Pringle J. E., Livio M., 2007, *MNRAS*, **376**, 1740
 Kudoh Y., Wada K., Norman C., 2020, *ApJ*, **904**, 9
 Lesur G., Ferreira J., Ogilvie G. I., 2013, *A&A*, **550**, A61
 Machida M., Nakamura K. E., Matsumoto R., 2006, *PASJ*, **58**, 193
 Mishra B., Begelman M. C., Armitage P. J., Simon J. B., 2020, *MNRAS*, **492**, 1855
 Parker E. N., 1958, *ApJ*, **128**, 664
 Pessah M. E., Psaltis D., 2005, *ApJ*, **628**, 879
 Ryan B. R., Gammie C. F., Fromang S., Kestener P., 2017, *ApJ*, **840**, 6
 Salvesen G., Armitage P. J., Simon J. B., Begelman M. C., 2016, *MNRAS*, **460**, 3488
 Scepi L., Lesur G., Dubus G., Flock M., 2018, *A&A*, **620**, A49
 Shakura N. I., Sunyaev R. A., 1973, *A&A*, **24**, 337
 Shlosman I., Begelman M. C., 1987, *Nature*, **329**, 810
 Sadowski A., 2016, *MNRAS*, **459**, 4397

Squire J., Quataert E., Hopkins P. F., 2024, Rapid, strongly magnetized accretion in the zero-net-vertical-flux shearing box ([arXiv:2409.05467](https://arxiv.org/abs/2409.05467)), <https://arxiv.org/abs/2409.05467>

Stone J. M., Hawley J. F., Gammie C. F., Balbus S. A., 1996, *ApJ*, **463**, 656

Stone J. M., Tomida K., White C. J., Felker K. G., 2020, *ApJS*, **249**, 4

Stone J. M., et al., 2024, *arXiv e-prints*, p. [arXiv:2409.16053](https://arxiv.org/abs/2409.16053)

Tetarenko B. E., Lasota J. P., Heinke C. O., Dubus G., Sivakoff G. R., 2018, *Nature*, **554**, 69

Trott C., et al., 2021, *Computing in Science and Engineering*, **23**, 10

Wang H.-Y., Guo M., Most E. R., Hopkins P. F., Lalakos A., 2025, *arXiv e-prints*, p. [arXiv:2504.03874](https://arxiv.org/abs/2504.03874)

Zhu Z., Stone J. M., 2018, *ApJ*, **857**, 34

This paper was built using the Open Journal of Astrophysics **L^AT_EX** template. The OJA is a journal which provides fast and easy peer review for new papers in the **astro-ph** section of the

arXiv, making the reviewing process simpler for authors and referees alike. Learn more at <http://astro.theoj.org>.